Bragg-Scattered Surface Plasmon Microscopy: Theoretical Study

Mana Toma, Wolfgang Knoll & Jakub Dostalek

Plasmonics

ISSN 1557-1955

Plasmonics
DOI 10.1007/s11468-011-9306-4

Springer

Your article is protected by copyright and all rights are held exclusively by Springer Science+Business Media, LLC. This e-offprint is for personal use only and shall not be self-archived in electronic repositories. If you wish to self-archive your work, please use the accepted author's version for posting to your own website or your institution's repository. You may further deposit the accepted author's version on a funder's repository at a funder's request, provided it is not made publicly available until 12 months after publication.

Springer

Author's personal copy

Plasmonics
DOI 10.1007/s11468-011-9306-4

Bragg-Scattered Surface Plasmon Microscopy: Theoretical Study

Mana Toma · Wolfgang Knoll · Jakub Dostalek

Received: 17 August 2011 / Accepted: 20 November 2011
© Springer Science+Business Media, LLC 2011

Abstract We present a new approach to surface plasmon microscopy with high refractive index sensitivity and spatial resolution that is not limited by the propagation length of surface plasmons. It is based on a nanostructured metallic sensor surface supporting Bragg-scattered surface plasmons. We show that these non-propagating surface plasmon modes are excellently suited for spatially resolved observations of refractive index variations on the sensor surface owing to their highly confined field profile perpendicular to as well as parallel to the metal interface. The presented theoretical study reveals that this approach enables reaching similar refractive index sensitivity as regular surface plasmon resonance (SPR) microscopy and offers the advantage of improved spatial resolution when observing dielectric features with lateral size <10 μm for the wavelength around 800 nm and gold as the SPR-active metal. This paper demonstrates the potential of Bragg-scattered surface plasmon microscopy for high-throughput SPR biosensing with high-density microarrays.

Keywords Surface plasmon resonance · SPR microscopy · SPR imaging · Diffraction grating · Biosensor

Introduction

Surface plasmon resonance (SPR) microscopy [1] that is also referred to as surface plasmon resonance imaging becomes an established optical method for the sensitive observation of (bio)interfaces [2–5] and particularly has been used for high-throughput detection and interaction analysis of biomolecules [6–8]. In these applications, surface plasmons (SPs) are resonantly excited along a metallic sensor surface to probe a two-dimensional microarray of spots with immobilized ligands. In most common implementations, SPR microscopy utilizes the Kretschmann configuration with a prism coupler [9, 10], an optically matched microscope objective lens [11] or diffraction gratings [12] for the excitation of SPs by an optical wave incident to a metallic sensor surface. Surface plasmons exhibit an electromagnetic field that is strongly confined at the metallic interface, and they are extremely sensitive to minute changes in the refractive index associated with the binding of target biomolecules to ligands tethered at the sensor surface. These variations alter the coupling strength to surface plasmons and lead to changes in the intensity of the reflected optical wave that is subsequently imaged at a detector. Typical SPR microscopy instruments can resolve refractive index (RI) changes as small as 10^{-5} refractive index units from arrays of spots with the characteristic size from tens to several hundreds of micrometers [13]. In order to further increase the accuracy (e.g., for the observation of binding of small molecules inducing low refractive index changes) and throughput (e.g., by using denser microarrays), these characteristics need to be improved.

Up to now, various approaches exploiting phase-contrast measurements [14], wide-field excitation of SP [4, 15], and surface plasmon modes propagating along strongly absorbing metals or at low wavelengths [3, 16, 17] were investigated to advance SPR microscopy. In general, these efforts demonstrated that enhancing the spatial resolution is accompanied with deteriorating RI resolution and vice versa. The reason is that the smallest measureable refractive index change

M. Toma · W. Knoll · J. Dostalek (✉)
Health and Environment Department,
AIT-Austrian Institute of Technology GmbH,
Muthgasse 11,
1190 Vienna, Austria
e-mail: jakub.dostalek@ait.ac.at

Published online: 21 December 2011

Author's personal copy

(RI resolution) is inversely proportional to the propagation length of surface plasmons L_p, while the smallest measureable lateral size of a dielectric feature in the direction to the SP propagation (spatial resolution) is proportional to L_p [17]. This inherent limitation of SPR microscopy can be overcome by employing non-propagating localized surface plasmons (LSPs) supported by metallic nanoparticles [18]. Unfortunately, sensors based on the spectroscopy of LSPs offer significantly lower RI resolution with respect to their counterparts relying in propagating SPs due to their small figure of merit [19].

In this paper, we investigate another approach that holds potential for simultaneously advancing both RI and spatial resolution of SPR microscopy. It is based on Bragg-scattered surface plasmons (BSSPs) supported by periodically modulated metallic surface on which counterpropagating SPs are diffraction-coupled [20]. The total length that these modes travel along the surface is comparable to regular SPs on flat metallic surface which does not compromise the high RI resolution [21]. However, their lateral confinement on the surface due to the repeated Bragg scattering holds potential for improving the spatial resolution [22]. In this study, we carry out numerical simulations to investigate the key characteristics of this new approach to SPR microscopy.

Optical Configuration

In what follows, we assume SPR microscopy based on the attenuated total reflection (ATR) method in the Kretschmann configuration depicted in Fig. 1a. A transverse magnetically (TM) polarized plane wave was made incident through a high refractive index glass prism at its base with a thin gold film. The angle of incidence θ was set close to that for which resonant coupling to surface plasmons occurs at the outer interface between the gold film and a low refractive index dielectric on its top:

$$\frac{2\pi}{\lambda} n_p \sin(\theta) = \mathrm{Re}\{\beta_{SP}\} = \frac{2\pi}{\lambda} \mathrm{Re}\left\{ \left(\frac{n_{Au}^2 n_w^2}{n_{Au}^2 + n_w^2} \right)^{1/2} \right\}, \qquad (1)$$

where λ is the wavelength, n_p is the refractive index of the prism, n_{Au} is the refractive index of the gold film, and n_w is the refractive index of the low refractive index dielectric. β_{SP} is a (complex) propagation constant of SP at an interface between a semi-infinite metal and a low refractive index dielectric. Re {} denotes the real part of a complex number. In further simulations, Cartesian coordinates were used with the x-axis lying parallel to the surface and in the plane of incidence, the y-axis perpendicular to the plane of incidence, and the z-axis perpendicular surface. The prism refractive

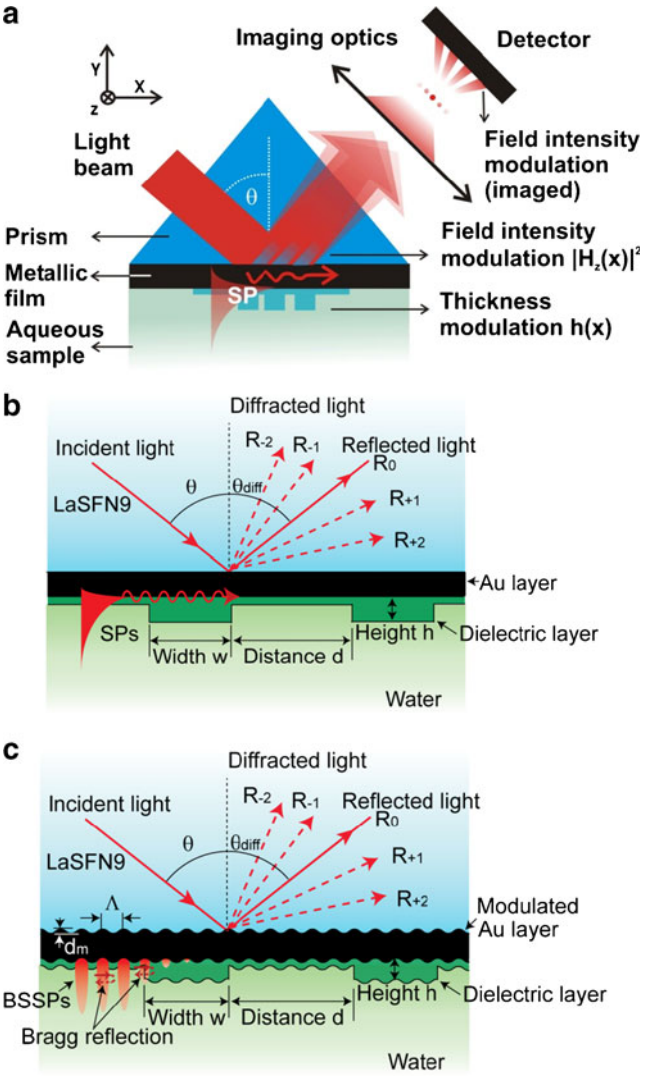

Fig. 1 **a** Schematics of the implementation of SPR microscopy based on ATR method with Kretschmann configuration utilizing **b** flat metallic film supporting regular surface plasmons and **c** periodically modulated metallic film supporting Bragg-scattered surface plasmons

index n_p was that of LaSFN9 glass [23]. A SPR-active gold film with the thickness of 50 nm and a refractive index n_{Au} taken from literature [24] was used. A dielectric film with a refractive index n_f=1.5 that is close to that of biomolecules [25] was attached on the gold surface, and its varied thickness $h(x)$ represented an object being imaged (e.g., an array of spots). The surface was brought in contact with semi-infinite aqueous medium with a refractive index of water n_w [26]. The gold film was assumed to be flat (for the excitation of regular SP, Fig. 1b) or with a sinusoidal relief modulation in the x direction with a periodicity of Λ= 280 nm and depth d_m=20 nm (for the excitation of BSSP, Fig. 1c).

The period of the modulation Λ was set to induce Bragg scattering of SP wave between wavelengths λ=750 and

Author's personal copy

800 nm. This period was obtained analytically from diffraction coupling condition (2):

$$\frac{2\pi}{\Lambda} = 2\mathrm{Re}\{\beta_{\mathrm{SP}}\} = \frac{4\pi}{\lambda}\mathrm{Re}\left\{\left(\frac{n_{\mathrm{Au}}^2 n_{\mathrm{w}}^2}{n_{\mathrm{Au}}^2 + n_{\mathrm{w}}^2}\right)^{1/2}\right\}. \quad (2)$$

As an object, a dielectric film with a periodically modulated height along the surface $h(x)$ was assumed in the following form:

$$h(x) = h_0 + \Delta h \sum_{n=-\infty}^{\infty} \vartheta(x + nL)\vartheta(w - x - nL), \quad (3)$$

where ϑ is a Heaviside step function, Δh is the height of a dielectric step, w is the lateral width of the dielectric step, L is the period, and n is an integer. Without the loss of generality, a thickness of the homogenous dielectric film of h_0=5 nm was chosen for the sake of improved convergence of the numerical model introduced in the next section. The dielectric layer thickness is varied only in one dimension that is parallel to the propagation of SP modes, and the characteristics of the imaging optics were omitted for simplicity.

Theoretical Model

The reflected field intensity variations along the inner metallic surface were calculated in the form of Rayleigh series for the probing of the sensor surface by regular SPs and BSSPs. As the probing optical wave was TM polarized, we calculated the changes in reflected magnetic field intensity with only non-zero component parallel to the surface H_z:

$$H_z(x) = \sum_{n=n_1}^{n_2} R_n \exp(+i\alpha_n x), \quad (4)$$

$$\alpha_n = \frac{2\pi}{\lambda} n_{\mathrm{p}} \sin\theta + \frac{2\pi}{L} n, \quad (5)$$

where R_n denotes the Rayleigh coefficient of the nth diffraction order. In the series (4), the sum over the diffraction orders from n_1 to n_2 was made to take into account diffraction orders propagating away from the metallic film through the glass medium at angles θ_{diff} between 0 and 90° (see Fig. 1b, c). The series of Rayleigh coefficients R_n were numerically solved by using finite element method that was implemented in a diffraction grating solver DiPoG (Weierstrass Institute, Germany). A grating in a computation cell with the length up to L=45 μm and height of 0.1 μm was approximated by a mesh of triangles (convergence was achieved for mesh with number of triangles larger than 40,000 for a flat gold film and 80,000 for a modulated gold film). Let us note that for structures supporting BSSPs, the periods L and Λ were adjusted to $L = p\Lambda$ holds for certain integer p. In the used numerical model, the set of Maxwell equations was solved by using the PARDISO solver of sparse linear systems (University of Basel, Switzerland).

In order to verify the validity of the used numerical model, we compared the numerical results with those obtained from an analytical theory described by Berger et al. [17]. We calculated the reflected magnetic field intensity distribution $|H_z(x)|^2$ at an inner gold interface when regular surface plasmons propagating along a flat gold surface probe a dielectric step (with a width of w=20 μm, distance of d=20 μm, and height of Δh=5 nm). As the analytical model is based on the assumption that SPs sequentially passing through individual walls of a dielectric step do not interact, we used the wavelength of λ=633 nm at which the propagation length of SPs is much shorter than the width of the used dielectric step w. Let us note that such numerical simulations would require increasing the dielectric step width w and thus significantly higher computing power for the wavelength λ=800 nm. The propagation length of SPs on a flat surface can be analytically calculated as:

$$L_{\mathrm{p}} = \frac{1}{2\mathrm{Im}\{\beta_{\mathrm{SP}} + \Delta\beta_{\mathrm{SP}}\}}, \quad (6)$$

and equals for the used structure to L_{p}=2.4 and 13 μm at wavelengths λ=633 and 800 nm, respectively. Let us note that Eq. 6 takes into account the radiation losses due to the finite thickness of gold film by the additional term of $\Delta\beta_{\mathrm{SP}}$ in the denominator (details can be found in [27]).

Results in Fig. 2 reveal an excellent agreement between analytical and numerical simulations. The intensity of the reflected plane wave hitting the surface with a dielectric step at an angle of incidence θ_{inc}=51.3° is modulated along the surface due to the varied coupling strength to SPs in areas

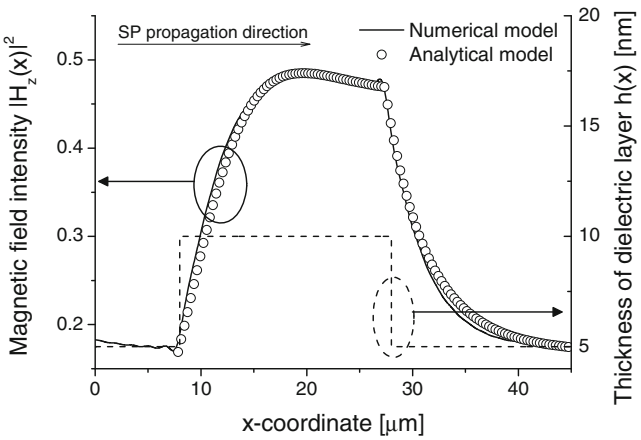

Fig. 2 Profile of the magnetic intensity $|H_z(x)|^2$ at the inner gold interface obtained by numerical and analytical models for a dielectric step at the outer gold film interface

Author's personal copy

with different thickness of the dielectric overlayer h. The changes of the field intensity distribution across dielectric step edges are not abrupt. The data show that the reflected field intensity $|H_z(x)|^2$ gradually increases and decreases when SP passes through the edge into the dielectric (x= 8 μm) or out of the dielectric overlayer (x=28 μm), respectively. The exponentially saturating increase is slightly modulated due to the interference of SPs propagating into the dielectric through the edge at x=8 μm and SPs that are excited through the metal at x>8 μm. This interference originates from the shift of the propagating constant β_{SP} due to variations of the dielectric layer thickness [28]. The field intensity exponentially decreases after SPs pass into water through the edge at x=28 μm with a decay constant $1/L_p$=0.49 μm^{-1} which agrees with the propagation length calculated from Eq. 6.

Results and Discussion

Bragg-Scattered and Regular Surface Plasmons

In further simulations, we used a wavelength λ~800 nm which was reported to provide the highest RI refractive index resolution in SPR biosensors with a flat gold film [29]. Firstly, dispersion relations of regular and Bragg-scattered surface plasmon modes were studied in vicinity to this wavelength by simulating the dependence of the reflectivity $|R_0|^2$ on the wavelength λ and the angle of incidence θ. Figure 3 shows the obtained reflectivity for (a) flat gold film supporting regular SPs and (b) for periodically modulated gold thin film supporting BSSPs. The gold surface was not covered with the dielectric layer $h_0=\Delta h=0$, and it was interfaced with a semi-infinite water medium. In the case of the flat gold film, regular SPs' dispersion is observed as a reflectivity drop located at angle θ that decreases from θ=50° to 48.5° when increasing the wavelength from λ=700 to 850 nm. These data are in accordance with the phase-matching condition (1).

For the modulated gold film, one can see a gap in the dispersion relation occurring at the wavelength band λ= 756–802 nm, where SPs cease propagating due to the Bragg reflections on the grating. At edges of the band gap, two new Bragg-scattered surface plasmon modes appear that are referred to as ω^+ (at λ=756 nm) and ω^- (at λ=802 nm) modes. The dispersion relation of BSSPs in Fig. 3 reveals that the spectral positions of these resonances are weakly dependent on the angle of incidence θ which is characteristic for non-propagating (localized) surface plasmon modes. These modes exhibit standing wave properties, and their electromagnetic field is concentrated either at the peaks (ω^-) or valleys (ω^+) of the metal layer relief modulation [20]. This phenomenon is illustrated in Fig. 4 which compares the profile of the electromagnetic field intensity through the layer structure for (a) regular SP, (b) BSSP ω^+, and (c) BSSP ω^-.

SPR Microscopy with Bragg-Scattered and Regular Surface Plasmons

In order to investigate key characteristics of SPR microscopy with regular and Bragg-scattered SPs, we carried out series of simulations of the optical response upon probing minute changes in the dielectric thin film thickness $h(x)$. We calculated the reflected magnetic field intensity distribution $|H_z(x)|^2$ at the inner gold interface and related the observed features to the height Δh, width w, and distance d between dielectric rectangular steps defined by Eq. 3. Regular SPs were excited by a plane wave with a wavelength of λ= 800 nm that was made incident on the gold surface under an angle θ=48.7°. BSSPs ω^- are excited by a plane wave with almost identical wavelength of λ=802 nm at an angle of incidence θ=51°. The ω^- was chosen as its excitation provides a field more confined to the metallic surface than

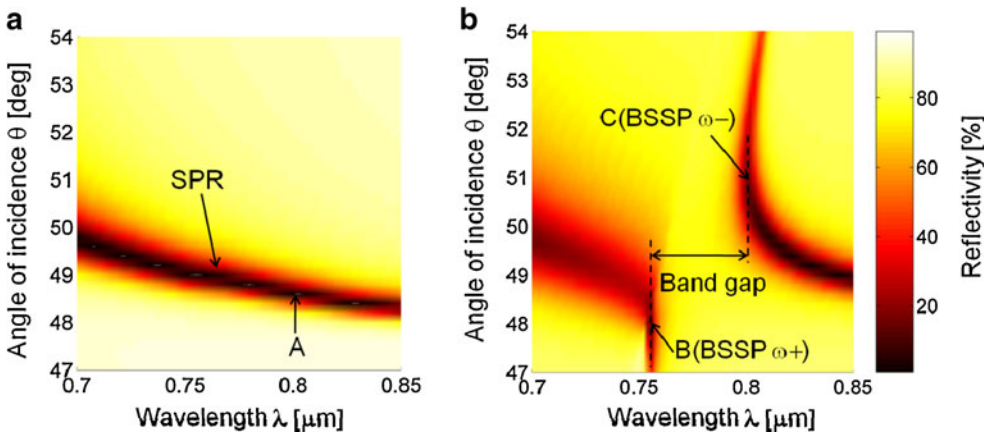

Fig. 3 Dispersion relation of surface plasmons propagating along **a** flat and **b** periodically modulated gold film in contact with water at the outer interface. The relief modulation of metallic film with the period of Λ= 280 nm and depth of d_m=20 nm were assumed

Author's personal copy

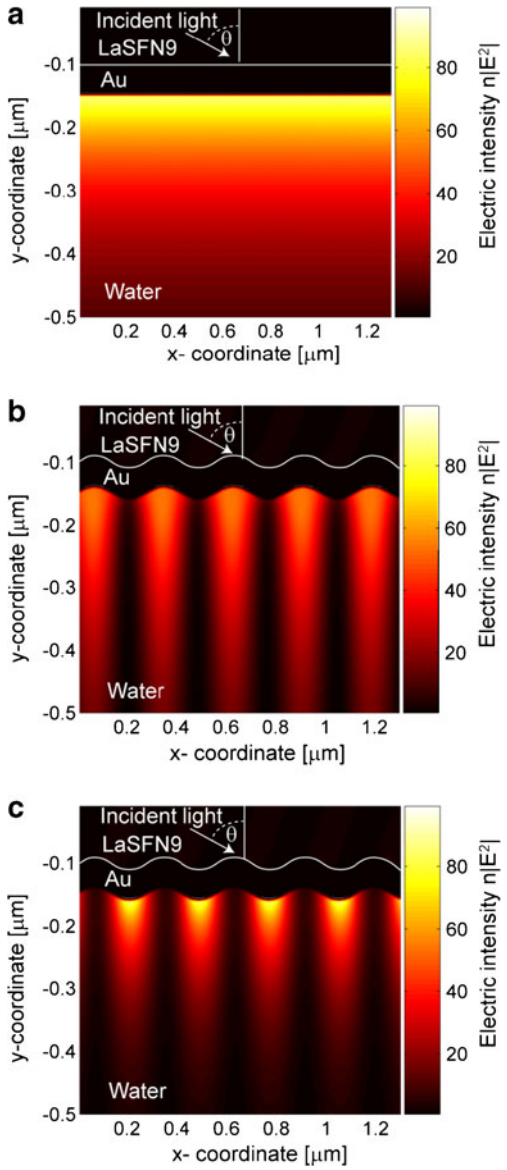

Fig. 4 Profile of field intensity at the outer gold surface for **a** regular SPs (*point A* in Fig. 3) and **b** ω^+ mode (*point B* in Fig. 3) and **c** ω^- mode (*point C* in Fig. 3) BSSPs

the ω^+ mode, see Fig. 3b, c. SP and BSSP ω^- modes were strongly excited at the gold surface with lower thickness $h(x)=h_0$ and weakly excited at areas with high thickness of a dielectric layer $h(x) = h_0 + \Delta h$. The reason is that the resonant wavelength of regular SP and BSSP modes is red shifted when increasing the refractive index, and the coupling to these modes becomes detuned. Additionally, BSSP ω^- moves into the band gap in the area covered with dielectric step $(h(x) = h_0 + \Delta h)$ in which SPs become strongly reflected on the grating.

The reflected magnetic field intensity $|H_z(x)|^2$ was firstly calculated for an array of dielectric rectangular steps with heights Δh=1, 2, and 3 nm, respectively, and with fixed width w=20 μm, distance d=25 μm, and computing period L=45 μm ($L = w + d$). As seen in Fig. 5a, for regular SPs, the magnetic field intensity distribution $|H_z(x)|^2$ exhibits a sawtooth profile with its minimum at the edge where SPs pass into the dielectric (x=9 μm) and its maximum at the edge where SPs pass from the dielectric (x=29 μm). As the height of the dielectric step Δh increases, both maximum and the minimum field intensities increase. These smearing effects are due to the small distance d and width w that are comparable to the propagation length L_p. Contrary to that, Fig. 5b shows that for the probing by BSSPs, the magnetic field intensity $|H_z(x)|^2$ reaches its maximum in the vicinity to the center of the dielectric step and exponentially decays to both sides away from the step. The maximum magnetic field intensity change $\Delta|H_z|^2$ linearly increases with the step height Δh, and the slope $\Delta|H_z|^2/\Delta h$ is approximately two-fold higher for regular SPs than for BSSPs ω^-. This indicates that for large objects with lateral size exceeding approximately 10 μm, SPR microscopy with regular SPs

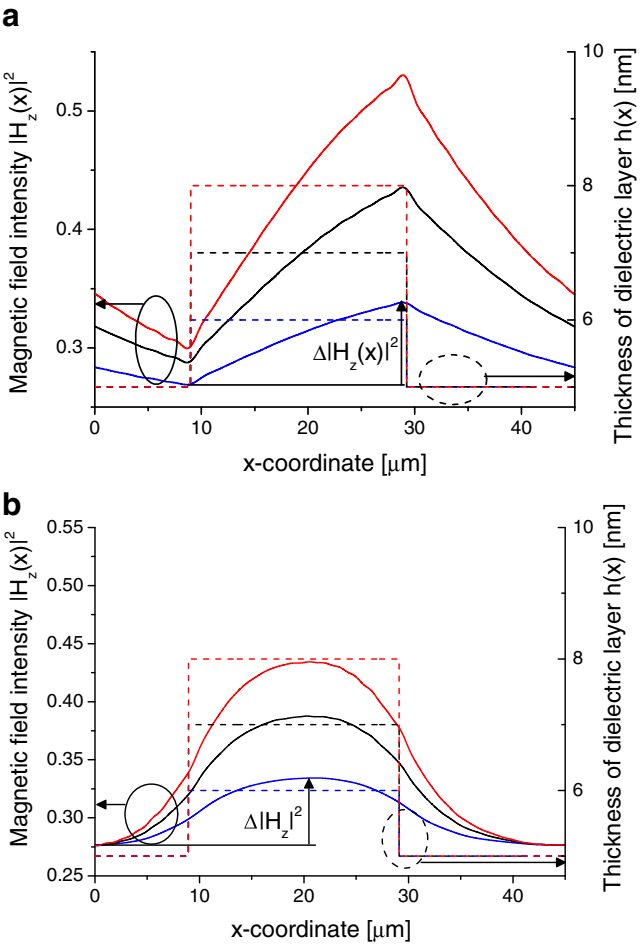

Fig. 5 The spatial dependence of reflected magnetic field intensity at the inner metal interface $|H_z(x)|^2$ on the height of the dielectric step for the structure supporting **a** regular SPs and **b** BSSPs ω^-

Author's personal copy

provides better refractive index sensitivity than that with BSSPs.

Afterwards, the dependence of the reflected magnetic intensity field distribution $|H_z(x)|^2$ on the width of a dielectric step (w=6.7, 11.2, and 20.2 μm) was calculated for a constant height Δh=2 nm and computing period L=45 μm. Figure 6 reveals that as the step width decreases, the width of associated feature in $|H_z(x)|^2$ also decreases. For the probing with regular SPs, the maximum field intensity change $\Delta|H_z|^2$ rapidly decreases when decreasing the dielectric step width w, and the distribution of $|H_z(x)|^2$ is asymmetrical with a slowly decreasing tail after the SP field passes through the edge from the dielectric to the water medium, see Fig. 6a. Contrary to these observations, Fig. 6b shows that $\Delta|H_z|^2$ is less dependent on the width step w when probed by BSSPs. In addition, the probing with BSSPs enables resolving small dielectric layer steps (with w<6 μm) with higher contrast (due to the higher maximum field intensity change $\Delta|H_z|^2$) than regular SPs. For such small dielectric features, the SPR microscopy with BSSPs takes clear advantage of the stronger lateral localization of the probing field. This can be quantified by the distance L_d between the maximum magnetic intensity field $|H_z(x)|^2$ and the position where $|H_z(x)|^2$ reaches half of its maximum. For BSSPs, L_d is approximately twice smaller (L_d=5.4 μm) than for regular SPs (L_d=10.3 μm).

Finally, the optical response was evaluated when two identical dielectric steps separated by different distances (d=9, 18, and 40.5 μm) were probed by regular SP and BSSP ω^-. The results presented in Fig. 7 were calculated for the width of steps of w=4.5 μm, height Δh=2 nm, and computation period L=45 μm. For regular SPs probing two dielectric steps brought in close proximity, the maximum intensities of the two associated peaks in $|H_z(x)|^2$ are significantly changed as the distance between neighboring steps gets closer. Contrary to these observations, the peaks in the magnetic field distribution $|H_z(x)|^2$ change negligibly for steps that are located at any distance from 9 to 40.5 μm when probed by BSSPs. This indicates that a strong cross

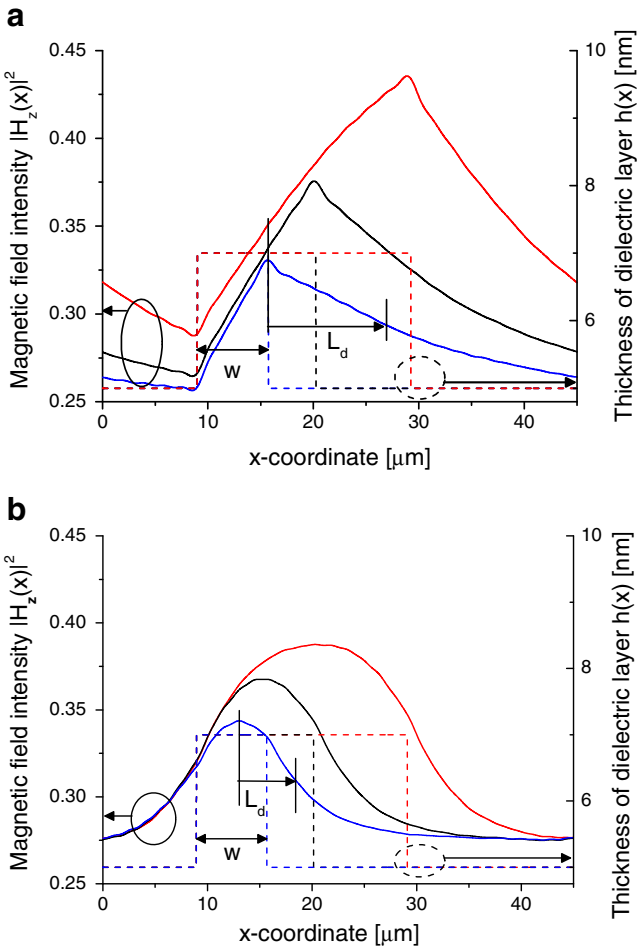

Fig. 6 The spatial dependence of reflected magnetic field intensity at the inner metal interface $|H_z(x)|^2$ on the width w of the dielectric step for the structure supporting **a** regular SPs and **b** BSSPs ω^-

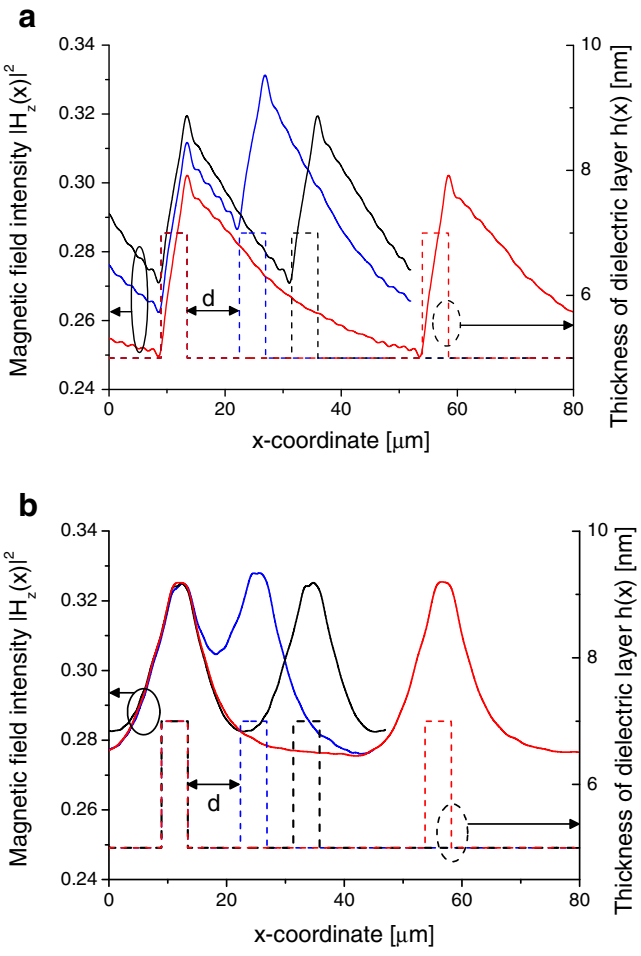

Fig. 7 The spatial dependence of reflected magnetic field intensity at the inner metal interface $|H_z(x)|^2$ on the distance between two neighboring steps in the dielectric film d upon probing by **a** regular SPs and **b** BSSPs ω^-

Author's personal copy

talk between neighboring sensing spots can be efficiently removed by using BSSP modes.

Conclusions

In this study, we introduced a finite element-based model for the investigation of spatial and refractive index resolution of SPR microscopy with flat and nanostructured metallic surfaces. In particular, we investigated the employment of densely periodically modulated gold surface supporting non-propagating Bragg-scattered surface plasmons for probing minute variations in the thickness of thin dielectric film. The presented simulations predict that this approach exhibits about two times lower refractive index resolution as regular SP microscopy when applied for the observation of large dielectric features with lateral size above 10 μm. However, for the observation of smaller features with lateral size <10 μm, we achieved an improved spatial resolution, contrast, and fidelity of the images by using BSSPs. For instance, when applied to the label-free readout of biomolecular interactions in microarray format, lower cross talk between neighboring spots will enable developing denser microarrays and thus enhancing throughput of the analysis. In addition, the smaller sensitivity of the excitation of BSSPs to changes in the angle of incidence holds potential for simplified instrumentation of SPR microscopy. Future efforts will be devoted to the implementation of the BSSP-based SPR microscopy that can be straightforwardly utilized by using nanoimprint lithography for the fabrication of a sensor chip which can be directly used with regular instruments for SPR microscopy.

Acknowledgments The authors would like to acknowledge the help of Dr. Roman Bruck in implementing DiPoG software on a Linux-based computation cluster. Support for this work was provided in part by the Center of Innovation and Technology of Vienna (ZIT) and the Austrian NANO Initiative (FFG and BMVIT) through the NILPlasmonics project within the NILAustria cluster (www.NILAustria.at).

References

1. Rothenhäusler B, Knoll W (1988) Surface–plasmon microscopy. Nature 332:615–617
2. Wang ZZ, Wilkop T, Han JH, Dong Y, Linman MJ, Cheng Q (2008) Development of air-stable, supported membrane arrays with photolithography for study of phosphoinositide–protein interactions using surface plasmon resonance imaging. Anal Chem 80:6397–6404
3. Giebel KF, Bechinger C, Herminghaus S et al (1999) Imaging of cell/substrate contacts of living cells with surface plasmon resonance microscopy. Biophys J 76:509–516
4. Jamil MMA, Denyer MCT, Youseffi M et al (2008) Imaging of the cell surface interface using objective coupled widefield surface plasmon microscopy. J Struct Biol 164:75–80
5. Scarano S, Mascini M, Turner APF, Minunni M (2010) Surface plasmon resonance imaging for affinity-based biosensors. Biosens Bioelectron 25:957–966
6. Smith EA, Corn RM (2003) Surface plasmon resonance imaging as a tool to monitor biomolecular interactions in an array based format. Appl Spectrosc 57:320–332
7. Boozer C, Kim G, Cong SX, Guan HW, Londergan T (2006) Looking towards label-free biomolecular interaction analysis in a high-throughput format: a review of new surface plasmon resonance technologies. Curr Opin Biotechnol 17:400–405
8. Lee HJ, Goodrich TT, Corn RM (2001) SPR imaging measurements of 1-D and 2-D DNA microarrays created from microfluidic channels on gold thin films. Anal Chem 73:5525–5531
9. Shumaker-Parry JS, Cambell CT (2004) Anal Chem 76:907–917
10. Johansen K (2005) Imaging SPR apparatus. US Patent 6862094
11. Huang B, Yu F, Zare RN (2007) Surface plasmon resonance imaging using a high numerical aperture microscope objective. Anal Chem 79:2979–2983
12. Singh BK, Hillier AC (2006) Surface plasmon resonance imaging of biomolecular interactions on a grating-based sensor array. Anal Chem 78:2009–2018
13. Yeatman EM (1996) Resolution and sensitivity in surface plasmon microscopy and sensing. Biosens Bioelectron 11:635–649
14. Piliarik M, Vaisocherova H, Homola J (2005) A new surface plasmon resonance sensor for high-throughput screening applications. Biosens Bioelectron 20:2104–2110
15. Stabler G, Somekh MG, See CW (2004) High-resolution wide-field surface plasmon microscopy. J Microsc-Oxf 214:328–333
16. Wark AW, Lee HJ, Corn RM (2005) Long-range surface plasmon resonance imaging for bioaffinity sensors. Anal Chem 77:3904–3907
17. Berger CEH, Kooyman RPH, Greve J (1994) Resolution in surface-plasmon microscopy. Rev Sci Instrum 65:2829–2836
18. Stewart ME, Mack NH, Malyarchuk V et al (2006) Quantitative multispectral biosensing and 1D imaging using quasi-3D plasmonic crystals. PNAS 103:17143–17148
19. Kvasnicka P, Homola J (2008) Optical sensors based on spectroscopy of localized surface plasmons on metallic nanoparticles: sensitivity considerations. Biointerphases 3:FD4–FD11
20. Barnes WL, Preist TW, Kitson SC, Sambles JR, Cotter NK, Nash DJ (1995) Photonic gaps in the dispersion of surface plasmons on gratings. Physical Rev B 51:11164–11168
21. Dostalek J, Adam P, Kvasnicka P, Telezhnikova O, Homola J (2007) Spectroscopy of Bragg-scattered surface plasmons for characterization of thin biomolecular films. Opt Lett 32:2903–2905
22. Lindquist NC, Lesuffleur A, Im H, Oh SH (2009) Sub-micron resolution surface plasmon resonance imaging enabled by nanohole arrays with surrounding Bragg mirrors for enhanced sensitivity and isolation. Lab on a Chip 9:382–387
23. SCHOTT AG (2011) Optical Glass Data Sheets, Germany
24. Homola J (2006) Surface plasmon resonance based sensors. Springer, Berlin
25. Voros J (2004) The density and refractive index of adsorbing protein layers. Biophys J 87:553–561
26. Palik ED (1998) Handbook of optical constants of solids. Elsevier, New York
27. Kretschmann E (1971) Die bestimmung optischer konstanten von metallen durch anregung von oberflächenplasmaschwingungen. Zeitschrift für Physik A Hadrons Nuclei 241:313–324
28. Rothenhausler B, Knoll W (1988) Surface plasmon interferometry in the visible. Appl Phys Lett 52:1554–1556
29. Piliarik M, Homola J (2009) Surface plasmon resonance (SPR) sensors: approaching their limits? Opt Express 17:16505–16517